https://doi.org/10.5194/egusphere-2026-5436
Preprint. Discussion started: 25 September 2026

Improving Reconstructed HY-1D/COCTS SST for Upwelling Events in the Gulf of Lion through Wind-Informed Cloud Detection

Zhuomin Li [1,2,3,4], Aida Alvera-Azcárate [4], Alexander Barth [4], Nathaniel Bensoussan[5], Lei Guan [2,3,6,*], and Na Xu [1]

[1]National Satellite Meteorological Center, China Meteorological Administration, Beijing, 100081, China
[2]Key Laboratory of Ocean Observation and Information of Hainan Province, Sanya Oceanographic Institution, Ocean University of China, Sanya, 572024, China
[3]College of Marine Technology, Faculty of Information Science and Engineering, Ocean University of China, Qingdao, 266100, China
[4]GeoHydrodynamics and Environment Research (GHER), University of Liège, Liège, 4000, Belgium
[5]Laboratoire d'Océanographie Physique et Spatiale (LOPS), IUEM, University of Brest, CNRS, Ifremer, IRD, 29280, Plouzané, France
[6] SANYA Oceanographic Laboratory, Sanya, 572024, China

Correspondence to: Lei Guan (leiguan@ouc.edu.cn)

Abstract. Sea surface temperature (SST) is essential for understanding ocean dynamics and air-sea interactions. SST from the Haiyang-1D (HY-1D) Chinese Ocean Color and Temperature Scanner (COCTS) has been obtained based on the algorithm derived using an atmospheric radiative transfer model. In the Gulf of Lion of the Mediterranean Sea, northwest winds prevail in summer and autumn, which favors upwelling events. This study aims to improve reconstructed HY-1D/COCTS SST for characterizing strong upwelling events in the Gulf of Lion. The study covers the period from May to November 2021(summer and autumn). The research area is 41°N–44°N and 3°E–8°E and the spatial resolution of COCTS SST is 1 km. Owing to persistent cloud cover, 61.92% of all pixels are missing. First, to better utilize COCTS SST, we apply Data Interpolating Empirical Orthogonal Functions (DINEOF) to reconstruct COCTS SST. The validation results for reconstructed COCTS SST show that DINEOF provides accurate statistical results on cloud pixels. We analyze the performance of the reconstructed COCTS SST in 8 sporadic upwelling events using the *in situ* data as reference. The hourly *in situ* data from 3 sites located in/nearby distinct upwelling areas from the Gulf of Lion (Marseille-Toulon area). The results show that the reconstructed COCTS SST characterizes most SST cooling events caused by upwelling, but not as intense as the *in situ* SST. Second, to overcome this limitation, we propose a wind-informed cloud detection procedure that takes into account wind speed and direction in order to improve the classification of upwelling-influenced pixels. The COCTS SST obtained by this improved cloud mask is subsequently reconstructed using DINEOF. The improved reconstructed COCTS SST has higher consistency with the *in situ* SST in the upwelling area. The results show the difficulty of cloud masking in areas with strong upwelling events and that the improved reconstructed HY-1D/COCTS SST, enabled by wind-informed cloud detection, have the potential to accurately describe such events.

https://doi.org/10.5194/egusphere-2026-5436
Preprint. Discussion started: 25 September 2026

1 Introduction

Sea surface temperature (SST) plays an important role in the complex interactions between sea and air. It is an important indicator for the upwelling and thermal structure of the ocean, and it affects the energy exchange in the air-sea coupling. SST is an essential variable for the understanding, monitoring, and predicting heat and gas fluxes. Haiyang-1D (HY-1D) is an operational ocean observation satellite, which is operated by National Satellite Ocean Application Service of China. The Chinese Ocean Color and Temperature Scanner (COCTS) on board can be used to observe SST. The two thermal infrared channels of COCTS for SST observation are channel 9 (10.30 ~ 11.30 μm) and channel 10 (11.50 ~ 12.50 μm).

For the SST observed by the infrared radiometer, clouds cover results in a large amount of missing data, which will affect the application of these SST data. Therefore, it is necessary to fill the gaps of infrared SST data. Several methods have been used to reconstruct missing data from SST images. Spline interpolation (Everson et al., 1997), optimal interpolation (He et al., 2003; Høyer et al., 2007), and deep learning methods (Su et al., 2026) are widely used to reconstruct SST datasets. Beckers and Rixen (2003) and Alvera- Azcárate et al. (2005) have developed an Empirical Orthogonal Functions (EOF) technique for filling the missing data. The method is called Data INterpolating Empirical Orthogonal Functions (DINEOF). DINEOF is a self-consistent data reconstruction technique with no required prior information and high efficiency (Beckers et al., 2003; Alvera-Azcárate et al., 2005).

The coastal upwelling is the wind-induced offshore movement of surface water, which is replenished with water from below (Kämpf & Chapman, 2016). Coastal upwelling supports the development of marine fisheries, having therefore a high relevance for society. The main driver of coastal upwelling is the wind (Bakun, 1973). When high wind speeds occur alongshore, and due to the Coriolis effect and Ekman transport, the depth-average transport is at a 90° angle from the direction of the sea surface wind (to the right in the northern hemisphere) under certain assumptions (in particular, constant turbulent viscosity). The reader is referred to Emerson et al.(2017) for more details. Therefore, the warm surface water moves away from the shore and is replaced by cooler deep water rising to the surface.

Several upwelling systems have been described, in particular the Eastern Boundary Upwelling Systems (EBUS), where the upwelling events happen due to dominant favorable surface alongshore winds, which includes the California, Humboldt, Canary, and Benguela current systems (García-Reyes et al., 2015). There are also sporadic wind-driven upwelling events occurring in other coastal ocean areas, such as the western coast of the South China Sea (Kuo et al., 2000; Li et al.,2025), the Southern Baltic Sea (Lehmann et al., 2008), the Banda Sea (Rachman et al., 2020), the coastal ocean area of southeast Australia (Rossi et al., 2014), Balearic Islands (Mourre et al., 2023) in the Mediterranean, and the central Mediterranean sea (Fragiacomo et al.,2022).

A 'full upwelling' is defined when the density interface rises towards the surface and reaches the sea surface causing a strong thermal signature (cooling) of 5-10°C during typical stratified summer conditions (Csanady, 1977). There are some studies demonstrating that were upwelling events occur in the Gulf of Lion and along the coasts of Provence (France, NW-Mediterranean Sea) under strong northwest winds for typically few days to maximum two weeks (Millot, 1979; Odic et al.,

https://doi.org/10.5194/egusphere-2026-5436
Preprint. Discussion started: 25 September 2026

2022; Thiébaut et al., 2024). When favorable wind speed up to 10 m/s develop, upwelling can happen along specific coastlines (upwelling areas) within one to two days, with the SST decreasing during the summer stratified season (Millot, 1979).

SST data are particularly well suited to study upwellings, given their surface signature. The upwelling on the western coast of the South China Sea was analyzed using the Advanced Very High Resolution Radiometer (AVHRR) SST (Kuo et al., 2000). The upwelling events in the San Matías Gulf (Northern Patagonia) were revealed by applying the AVHRR SST data (Pisoni et al., 2014). The spatial and temporal distribution of the upwelling on the southeastern coast of Australia was mapped by applying the monthly MODIS SST data (Huang et al., 2019). The upwelling in the Eastern Aegean Sea was detected by MODIS SST from Terra and Aqua (Ciappa, 2019). The coastal upwelling in the east of Taiwan Island was mapped using the Himawari-8 SST data (Huang et al., 2021). Multiscale Ultrahigh Resolution (MUR) L4 analysis SST produced from infrared and microwave SST was used to analyze the upwelling in the Gulf of Guinea (Wiafe et al., 2015). However, there are some limitations when we apply the infrared SST or analysis SST to analyze intermittent upwelling systems. For L3 SST, the cloud cover can limit the availability of the infrared SST data, which may miss the SST cooling observation. In addition, there may be spurious cloud flags for L3 SST data and strict quality control for L4 SST data, resulting in the intensity underestimation of the upwelling events and limitations in accounting for their spatial and temporal extents (von Schuckmann et al. 2019, Meneghesso et al., 2020).

In this research, the high-intensity events from the Marseille and Toulon upwelling areas are characterized by analyzing the time-series of *in situ* and satellite SST data. In this paper, COCTS L2 SST refers to the swath SST, COCTS L3 SST denotes the daily SST generated by projecting the COCTS L2 SST data, and COCTS L4 SST represents the gap-free SST reconstructed from COCTS L3 SST applying the DINEOF method. HY-1D/COCTS L3 SST in the Gulf of Lion is reconstructed by applying the DINEOF to fill in the pixels with cloud cover. the response of reconstruction HY-1D/COCTS L4 SST to the strong upwelling events is analyzed. The cloud detection processing is improved for the COCTS L3 SST data in terms of retaining more available cold pixels flagged as cloud. The performance of the improved reconstructed COCTS L4 SST in the same strong upwelling events is also analyzed.

2 Material and Methods

2.1 Data

The study period is from May to November 2021, and the spatial extent is the Gulf of Lion. COCTS L3 SST is obtained by projecting COCTS L2 SST into the images with grids of 0.01°×0.01°. The COCTS L2 SST is retrieved based on the atmospheric radiative model, which is skin temperature (Li et al., 2023). The nadir resolution is 1.1 km. The width of COCTS L2 SST image is 2900 km. COCTS provides twice-daily observations, with daytime and nighttime overpasses for the same location. For the COCTS SST in the daytime and nighttime, the global bias between COCTS SST and *in situ* SST quality monitor (iQuam) data from May to November in 2021 is -0.11°C, and the standard deviation is 0.54°C for 65,378

https://doi.org/10.5194/egusphere-2026-5436
Preprint. Discussion started: 25 September 2026

matchups. The bias between COCTS SST and VIIRS SST is 0.03°C, and the standard deviation is 0.53°C for 4,455,678,619 matchups (Li et al., 2023). The cloud detection was performed by applying brightness temperature and brightness temperature difference value, uniformity information, and difference between COCTS L2 SST and OSTIA SST. For the daytime, the reflectance was added (Li et al., 2023). For all pixels, quality levels are defined as follows: the land and ice pixels are flagged as quality level 0; the cloud pixels are flagged as quality level 1; the pixels with large difference from reference SST are flagged as quality level 2; the pixels with bad uniformity are flagged as quality level 3; and the pixels near the cloud pixels and the pixels with large satellite zenith angle are flagged as quality level 4; and the pixels with quality level 5 have the best accuracy (Li et al., 2023). Only the COCTS SST in the nighttime is reconstructed using DINEOF, because the diurnal warming signal may interfere with the study of upwelling. Fig. 1 shows the COCTS SST over the Mediterranean Sea, together with the geographic location of the Gulf of Lion (inside the black-outlined box).

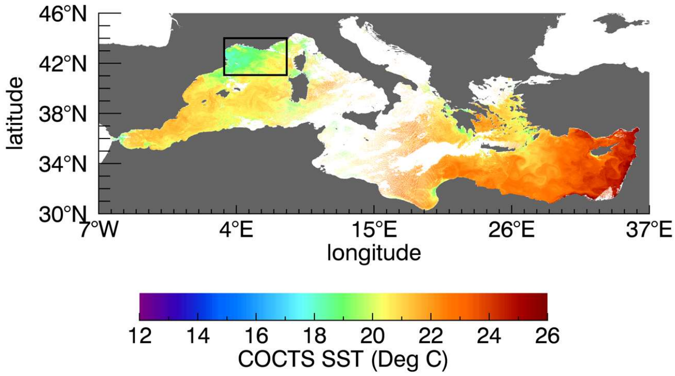

Figure 1: The COCTS SST over the Mediterranean Sea and the geographic location of the Gulf of Lion (inside the black outlined box)

The *in situ* data are from the T-MEDNet coastal observation network database (Bensoussan et al. 2019, Garrabou et al., 2019), which is a platform that tracks climate change effects in the Mediterranean. T-MEDNet (www.t-mednet.org) aims to establish a network of observations on the impacts of climate change on Marine coastal ecosystems and to promote standard monitoring programs for obtaining large-scale and long-term sea temperature and biological indicators (Garrabou et al., 2019). Local temperatures in long time series are acquired using HOBO U22 Water Temp Pro v2 data loggers (with an accuracy of 0.2°C), which is set by divers along rocky walls or buoys. The temperature sensor is set to collect hourly data, and the available observation depth is from the depth of 5 m to 40 m, and the observation is made every 5 m. Loggers and data are retrieved every 6 months or every year. In this study, *in situ* SST from three sites named Marseille-Riou, Cassis, and CapVieux is used. The geographic positions of the three sites are 43.17°N and 5.39°E, 43.02°N and 5.56 °E, 43.04°N and 5.84°E, respectively. The positions of the three sites are shown in Fig. 2. They are under the direct influence of two distinct upwelling source points forced by the same synoptic winds, but with modulations due to topo-bathymetric features and

https://doi.org/10.5194/egusphere-2026-5436
Preprint. Discussion started: 25 September 2026

local-scale wind heterogeneities. The first is the Cassidaigne upwelling source point (sites 1 & 2), which is the most active for the NW-Mediterranean Sea in terms of Ekman offshore transport (total duration and intensity of the events (Odic et al, 2022). The second is the Toulon source point (sites 3).

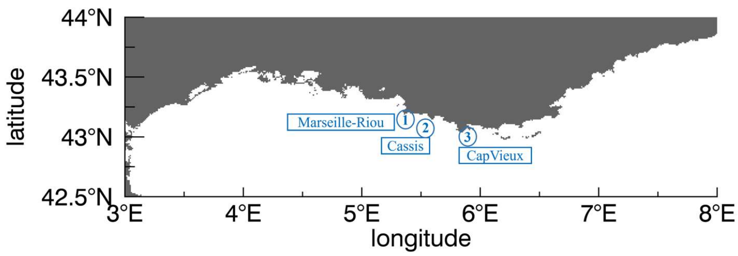

Figure 2: The positions of the three *in situ* sites using in the study.

The wind speed data used in this research is the Global Ocean Hourly Reprocessed Sea Surface Wind from Scatterometer and Model (10.48670/moi-00185), which is downloaded from the Copernicus Marine Environment Monitoring Service (CMEMS). The hourly wind speed data has a spatial resolution of 0.125° × 0.125°, and it includes the northward and the eastward wind. The CMEMS wind speed data is the adjusted ERA5 reanalysis data from the European Centre for Medium-Range Weather Forecast (ECMWF), which is corrected by applying the hourly bias with the wind speed data from satellite observation data such as Metop-A, Metop-B, Metop-C, and the Advanced Scatterometer (ASCAT) wind speed data.

The Operational Sea Surface Temperature and Sea Ice Analysis (OSTIA) system generates global, daily, gap-filled foundation SST fields at 0.05°×0.05°(10.48670/moi-00165, Good et al., 2020). These data are obtained from the CMEMS catalog. OSTIA SST data is produced by using high-accuracy multi-mission SST containing infrared, microwave, and drifting or moored measurements (Good et al., 2020).

iQuam data is processed and distributed by the National Oceanic and Atmospheric Administration (NOAA) National Environmental Satellite, Data, and Information Service (NESDIS) Center for Satellite Applications and Research (STAR) (https://www.star.nesdis.noaa.gov/socd/sst/iquam/data.html), including SST data from conventional ships, drifters, coastal and drifter moorings, Argo floats, high-resolution drifters, integrated Marine observing system ships, and coral reef watch buoys (Xu et al., 2014). The iQuam performs quality controls *in situ* SST from the Global Telecommunication System (GTS) data, applying buddy checks, Bayesian reference, data deduplication, SST spike checks, plausibility checks, and platform track checks (Xu et al., 2014). The data with the highest quality level of 5 is used.

2.2 Strong upwelling events in the Gulf of Lion

We use the *in situ* data in the Marseille-Riou site from May to November 2021 to detect and characterize upwelling events. Fig. 3 shows *in situ* temperature changes over time and depth in Marseille-Riou site.

https://doi.org/10.5194/egusphere-2026-5436
Preprint. Discussion started: 25 September 2026

This study focuses on upwelling events characterized by cold water rising to a depth of at least 5 m, with the analysis restricted to cases where the following two conditions are simultaneously satisfied:

1. The temperature at 5 m depth is at least 5°C colder than the maximum temperature for the month it's in.
2. The difference between the temperature at 5 m and 10 m is less than 2°C.

Table 1 shows the 8 events defined in this research, totally 42 days.

Table 1: The 8 events defined in this research.

Event	Start date	End date	Duration in days
1	June 26	June 27	2
2	June 30	July 6	7
3	July 14	July 20	7
4	August 2	August 12	11
5	August 17	August 20	4
6	August 28	August 31	4
7	September 20	September 24	5
8	October 7	October 8	2

Fig. 4 shows the wind speed on August 28 and the COCTS L3 SST on August 30. For the wind speed image, the color represents the value of the wind speed calculated by northward and eastward wind speed, and the gold arrows represent the wind norm and direction. We can see there is a strong northwest wind speed of more than 10 m/s in most of the area, which is a driving factor in the occurrence of upwelling in the coming days (events 6), the SST image shows that there is an obvious SST cooling phenomenon near-land (the green and light blue area).

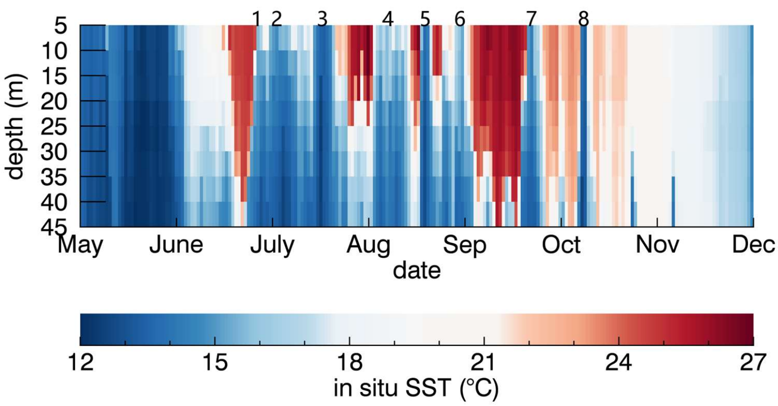

Figure 3: The *in situ* temperature change over time and depth (5-40m) in Marseille-Riou site from May to November in 2021.

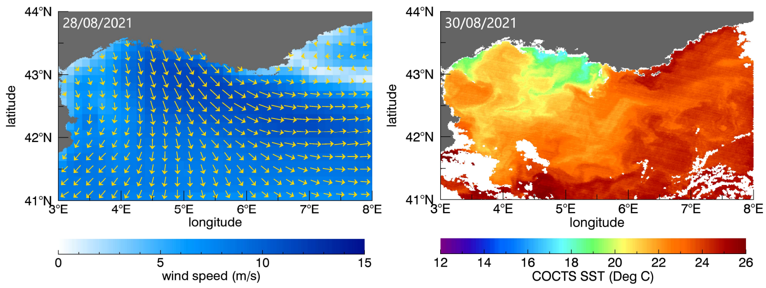

(a) (b)

Figure 4: Wind speed and COCTS SST on upwelling events(a) Wind speed (colors) and direction (arrows) on August 28 (b) COCTS SST on August 30.

2.3 Reconstruction of the COCTS SST

COCTS L3 SST is reconstructed by applying DINEOF. DINEOF is a statistical method based on EOFs, which is used to fill in incomplete data. Eigenvalues and eigenvectors are obtained through EOF analysis, the optimal reconstruction order of EOF is determined through cross-validation, and the values of missing pixels can be inferred (Alvera- Azcárate et al.,2005). When using DINEOF for data reconstruction, the data should be arranged into a two-dimensional matrix X, the size of which is $m \times n$, where m is the spatial dimension and n is the temporal dimension. The valid data are subtracted from the average of X. Missing data pixels are marked, and the values of missing pixels in the original data are set to 0 (Alvera- Azcárate et al.,2005). Singular Value Decomposition (SVD) is performed for X. The process is repeated until the convergence condition is met. The optimal EOF model obtained through multiple iterations can represent the spatial and temporal characteristics of data to the greatest extent and can provide more accurate reconstruction results for missing data. Convergence is achieved when the ratio of the root mean square errors between consecutive iterations of reconstructed missing data becomes lower than 0.001 times the standard deviation of existing data, we consider that it is convergent.

The accuracy of the COCTS SSTs before and after reconstruction are described and the performance of the COCTS SST in strong upwelling events is analyzed combined with the *in situ* SST in Section 3.

3 Results and Discussion

3.1 The reconstruction of COCTS SST in the Gulf of Lion

For the COCTS SST reconstruction, only the SST values with the quality level of 4 and 5 are retained. The overall availability of the COCTS L3 SST in the Gulf of Lion is 38% in terms of spatial coverage within the study period. The COCTS L3 SST images with an availability of less than 2% (spatial dimension) are removed and will not be reconstructed, and the pixels with an availability of less than 2% (time dimension) are considered as invalid pixels and will not be

https://doi.org/10.5194/egusphere-2026-5436
Preprint. Discussion started: 25 September 2026

reconstructed. A total of 187 out of the 214 COCTS SST images meet the conditions and are input to DINEOF. The number of optimal EOF modes for the DINEOF reconstruction is 9. Fig. 5 shows the COCTS SST images before and after reconstruction with availabilities of 6% and 45% , respectively. In terms of the consistency of images before and after reconstruction, it can be seen that DINEOF performs well in COCTS SST images both in lower and higher availabilities. The reconstructed COCTS SST is referred as COCTS L4 SST in the following.

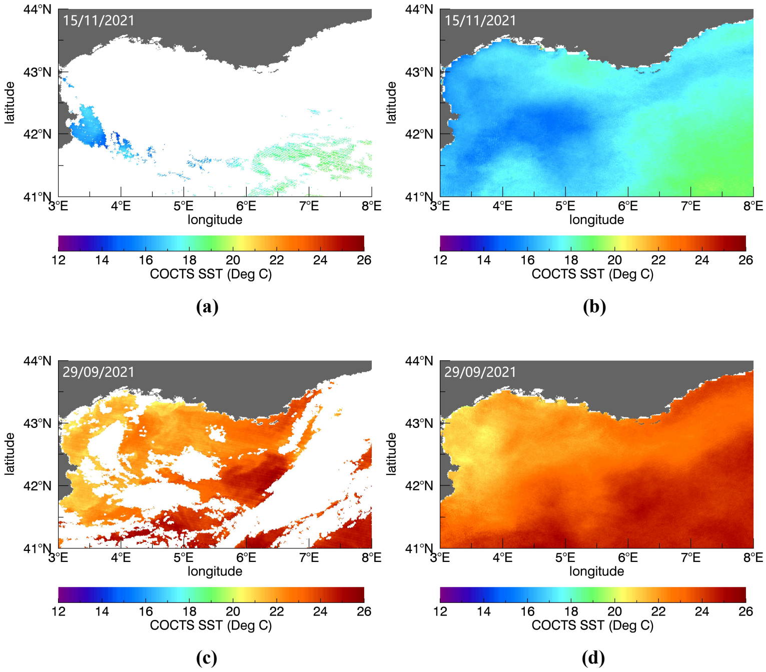

Figure 5: The COCTS SST images before and after reconstruction with different availabilities. (a) and (b) are the COCTS SST images on November 15, 2021, with an availability of 6%, (c) and (d) are the COCTS SST images on September 29, 2021, with an availability of 45 %.

The reconstructed COCTS L4 SST is compared with the highest-quality iQuam SST with a temporal window of 12 h and a spatial window of 1 km. Table 2 shows the difference between the COCTS SST and iQuam SST. The STD represents the standard deviation, the Med. represents the Median, the RSD represents the robust standard deviation (1.4826 × median(|x_i− median(x)|), where x_i denotes each element in the full set of differences x), and the No. is the Number. The bias of clear pixels before DINEOF is 0.01°C, and the standard deviation is 0.59°C, which is not as good as the validation results of the global COCTS L2 SST (Li et al., 2023). This may be due to the increase in the time window (12 h rather than 1 h for COCTS L2 SST) and the relatively lower accuracy of the near-land SST. The bias of the clear pixels after DINEOF is 0.03 °C, and the standard deviation is 0.58 °C. After reconstruction, an additional 1660 pixels are matched against the iQuam

https://doi.org/10.5194/egusphere-2026-5436
Preprint. Discussion started: 25 September 2026

data, and the bias of cloud pixels after DINEOF is -0.11 ℃, and the standard deviation is 0.67 ℃. Fig. 6 shows the spatial distribution of the difference between the COCTS and iQuam SSTs, we can see although most of the matchups are distributed in the relatively lower latitude, there are also some near-land matchups, which display the good performance of the reconstruction process. Fig. 7 shows the scatter plot of COCTS and iQuam SSTs, it can be seen that the reconstructed COCTS SST have high consistency with iQuam SST for both clear and cloud pixels. The results show that the accuracy of the reconstructed COCTS L4 SST is acceptable for the application.

Table 2: The difference between the COCTS SST and iQuam SST.

	Bias (℃)	STD (℃)	Med. (℃)	RSD (℃)	No.
clear pixels before DINEOF	0.01	0.59	0.01	0.53	914
clear pixels after DINEOF	0.03	0.58	0.04	0.54	914
cloud pixels after DINEOF	-0.11	0.67	-0.10	0.67	1660

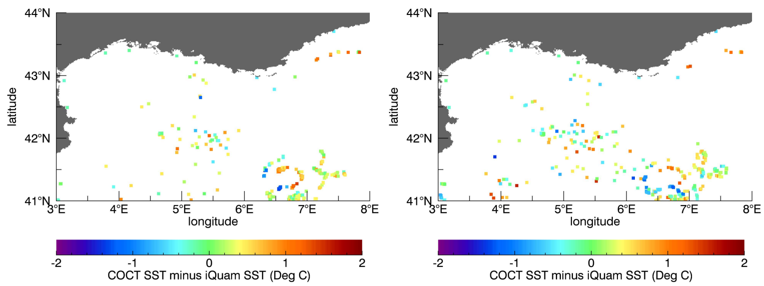

(a) (b)

Figure 6: The spatial distribution of the difference between the COCTS and iQuam SSTs (a) clear pixels (b) cloud pixels.

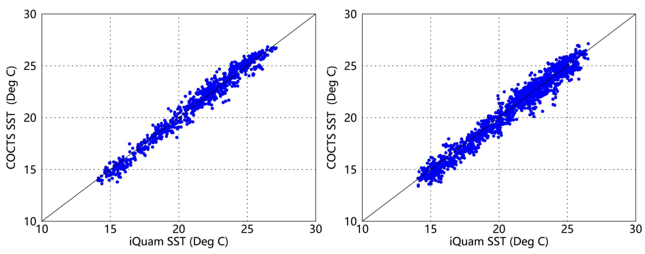

(a) (b)

Figure 7: The scatter plot of COCTS and independent iQuam SSTs (a) clear pixels (b) cloud pixels.

https://doi.org/10.5194/egusphere-2026-5436
Preprint. Discussion started: 25 September 2026

3.2 The performance of the reconstructed COCTS SST for strong upwellings

The performance of the reconstructed COCTS in strong upwelling events is analyzed. Fig. 8 shows the time series of the COCTS SSTs before and after reconstruction and the *in situ* SST. As expected, we can see that compared to the COCTS L3 SST, there is much more available data from the reconstructed COCTS L4 SST in this period, increasing from 30 to 187 in site 1. The reconstructed COCTS L4 SST is consistent with the COCTS L3 SST, and it is also consistent with the *in situ* SST outside the blue areas. However, there are large differences between the reconstructed COCTS L4 SST and the *in situ* SST during strong upwelling events. In event 3 of Fig. 8, the reconstructed COCTS L4 SSTs are relatively close to the *in situ* SSTs at Marseille-Riou and Cassis sites, the maximum of the differences are around 1°C at the Marseille-Riou site, 1°C at the Cassis site, but around 4°C at the CapVieux site, respectively. However, event 7 shows the largest differences among all events between the reconstructed COCTS L4 SSTs and the *in situ* SSTs, with maximum differences exceeding 5℃ at all three sites. For most of the events, there are differences of 2 to 4 °C between the reconstructed COCTS L4 SSTs and the *in situ* SSTs at the three sites.

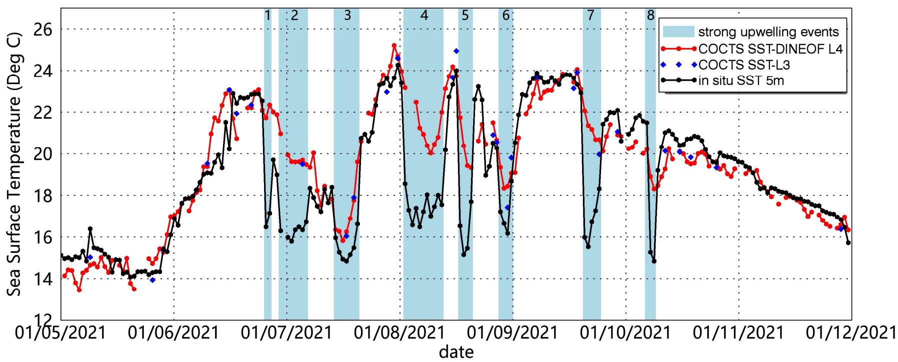

(a)

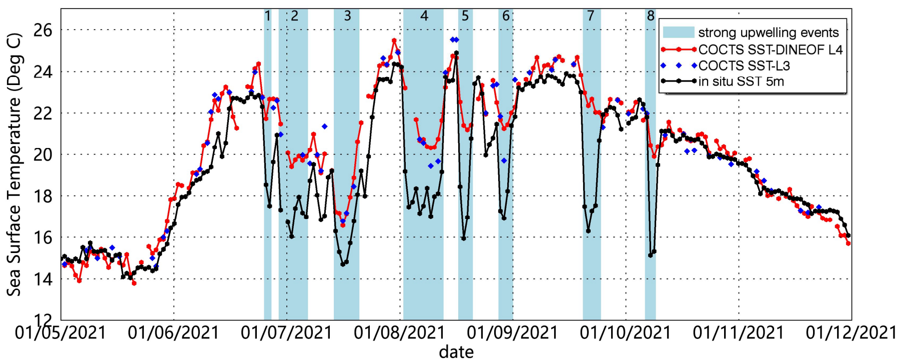

(b)

https://doi.org/10.5194/egusphere-2026-5436
Preprint. Discussion started: 25 September 2026

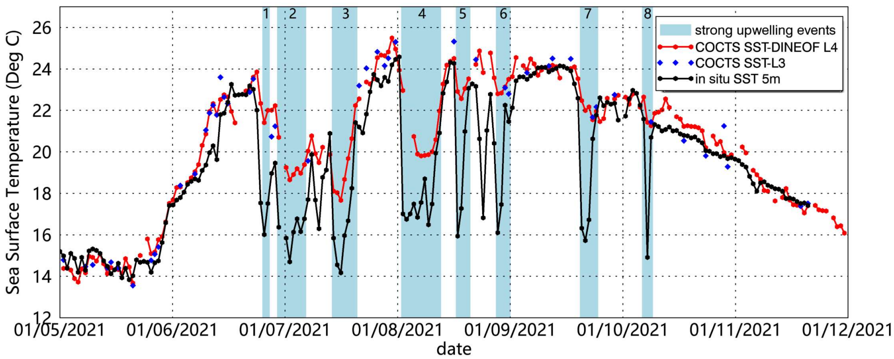

(c)

Figure 8: The time series of the COCTS SSTs before and after reconstruction and the *in situ* SST (a) Marseille-Riou (b) Cassis (c) CapVieux.

The results show that the COCTS L3 SST and reconstructed COCTS L4 SST both perform not very well when strong upwelling events happen. Although they characterize most of the SST cooling events caused by the strong upwelling, but not as intense as the *in situ* SST at the depth of 5 m. This may be due to the flagging of the cooling SST in satellite measurements or just the different responses of skin temperature and bulk temperature to the strong upwelling events. But for the second reason, when the wind speed is high, there will not be such a large difference between skin temperature and the bulk SST. Fig. 9 shows the COCTS L3 SST before and after cloud detection and the OSTIA SST on August 18, 2021 and October 8, 2021, which are in event 5 and event 8 respectively. From the images in Fig. 9, we can see in the near-land area, some upwelling pixels are misidentified as cloud pixels due to the values of OSTIA SST. The cloud detection process in the nighttime mainly includes the Brightness Temperature (BT) difference between the two infrared channels, the local standard deviations of the BT, and the difference between the COCTS SST and the OSTIA SST (Li et al., 2023). The last one may mostly contribute to the present results. Therefore, we analyze how the OSTIA SST performs in upwelling events in this area, to judge if the difference with OSTIA flags most of the cooling SST due to the upwelling. On the other hand, the OSTIA SST is the foundation SST (Good et al., 2020), so we can judge if it is more consistent with *in situ* SST. Fig. 10 shows the time series of COCTS SSTs before and after reconstruction, *in situ* SST, and OSTIA SST at the Marseille-Riou site. The OSTIA SST is more consistent with the COCTS SSTs rather than the *in situ* SST when there are upwelling events. This may be because only high-quality SST data from both satellite and *in situ* sources are assimilated into the OSTIA production system, which also employs rigorous quality control procedures (Good et al., 2020), resulting in a similar performance with the COCTS SST in upwelling events. According to the previous research, there was also a larger positive bias of OSTIA and the *in situ* SST in upwelling events and areas than normal (Meneghesso et al., 2020). Therefore, the threshold of the difference between COCTS SST and OSTIA SST is just -1.2℃ (following Li et al., 2023), which removes most of the cold pixels due to the upwelling.

https://doi.org/10.5194/egusphere-2026-5436
Preprint. Discussion started: 25 September 2026

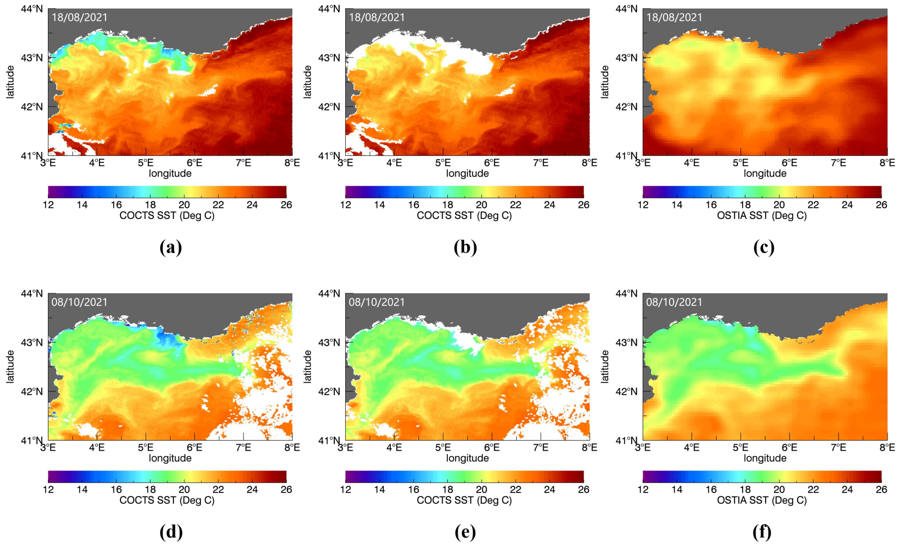

Figure 9: The COCTS L3 SST before (a) and after (b) cloud detection and the OSTIA SST (c) on August 18 and respectively (d), (e) and (f) for October 8.

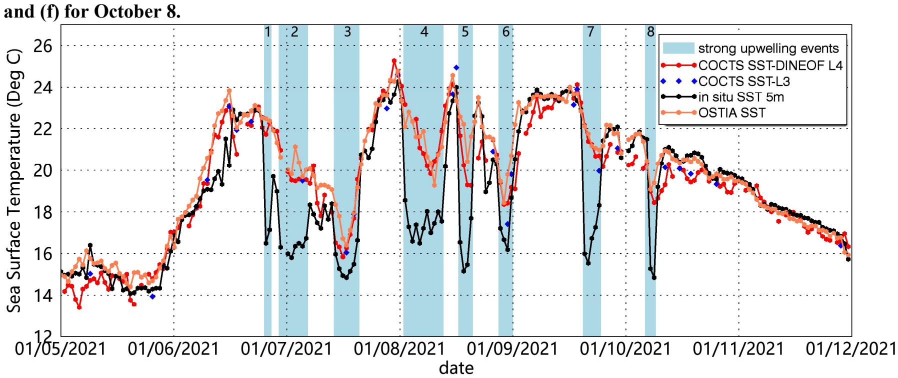

Figure 10: The time series of COCTS SSTs before and after reconstruction, *in situ* SST, and OSTIA SST at the Marseille-Riou site.

3.3 Improvement for the COCTS SST

3.3.1 The relationship analysis between different SSTs and alongshore wind speed at the Marseille-Riou site

To preserve SST cooling pixels induced by upwelling that are incorrectly identified as clouds, Upwelling events have a high relationship with wind speed, and the SST cooling following an upwelling-favorable wind speed event usually has a delay of 6 to 54 hours (Odic et al., 2022). According to the Ekman dynamics, we focus on the alongshore wind speed. The alongshore

https://doi.org/10.5194/egusphere-2026-5436
Preprint. Discussion started: 25 September 2026

wind speed is calculated from the northward wind speed, eastward wind speed, and the direction of the coastline calculated by the land mask. Fig. 11 shows the time series of COCTS SSTs with and without cold pixels, *in situ* SST, OSTIA SST, and alongshore wind speed at the Marseille-Riou site. Pixels with COCTS SST values below 5°C are excluded to eliminate obvious cloud contamination. The purple points represent the COCTS L3 SST without cloud flags (the cold pixels may be cloud-covered pixels or the upwelling-influenced pixels) and the green line represents the alongshore wind speed, which is the maximum alongshore wind speed in the window of 54 hours before the SST (Odic et al., 2022). The 54 hours is the longest delay in SST cooling relative to the upwelling-favorable wind. In all upwelling events, the alongshore wind speed is strong, from 5 m/s to more than 10 m/s, and the COCTS L3 SST with cold pixels is more consistent with the *in situ* SST in all upwelling events, but there are other obvious cloud pixels outside the upwelling events (The two purple pixels between events 6 and 7, with the SST values of around 5°C). Fig. 12 shows the differences between COCTS L3 SST with cold pixels and OSTIA SST marked by purple points, as well as the differences between OSTIA SST and *in situ* SST marked by pink points. In the upwelling events, COCTS SST has a negative deviation from OSTIA SST, and OSTIA SST has a positive deviation from the *in situ* SST, the two differences are distributed almost symmetrically on both sides of the line where the difference is zero in most of the days. Fig. 11 and 12 suggest that the difference between COCTS SST and OSTIA SST causes the SST cooling pixels to be flagged in upwelling events, although they are close to the *in situ* SSTs. From Fig. 12, we also find that the difference between COCTS SST and OSTIA SST may have a relationship with the alongshore wind speed. For instance, in event 6, the wind speed is less than 9m/s, and the difference between COCTS SST and OSTIA SST is greater than -2.5°C. However, events 4, 7, and 8 with strong wind speed greater than 10 m/s, correspond to the larger difference between COCTS SST and OSTIA SST, which is -4°C or -5°C. There is a negative correlation between them.

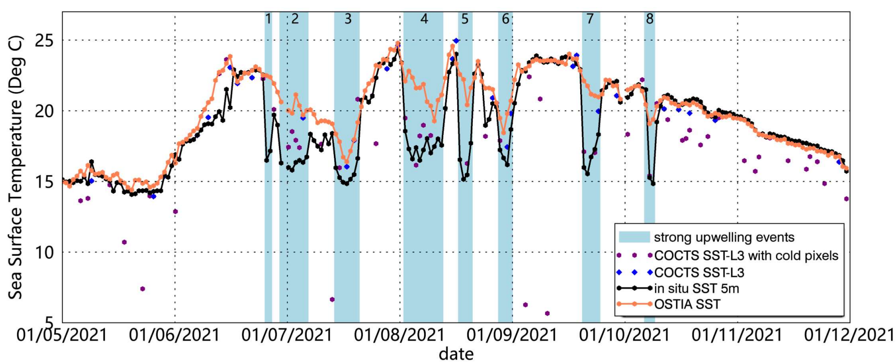

(a)

https://doi.org/10.5194/egusphere-2026-5436
Preprint. Discussion started: 25 September 2026

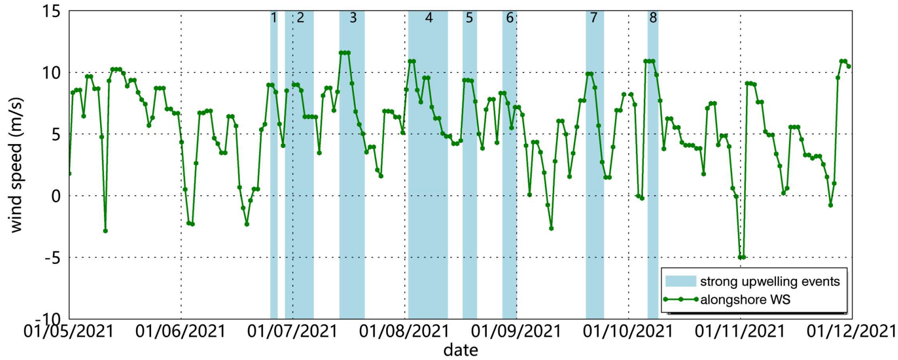

(b)

Figure 11: The time series of COCTS SSTs with and without cold pixels, *in situ* SST, OSTIA SST, and alongshore wind speed at the Marseille-Riou site (a) COCTS SSTs with and without cold pixels, *in situ* SST, OSTIA SST (b) Alongshore wind speed.

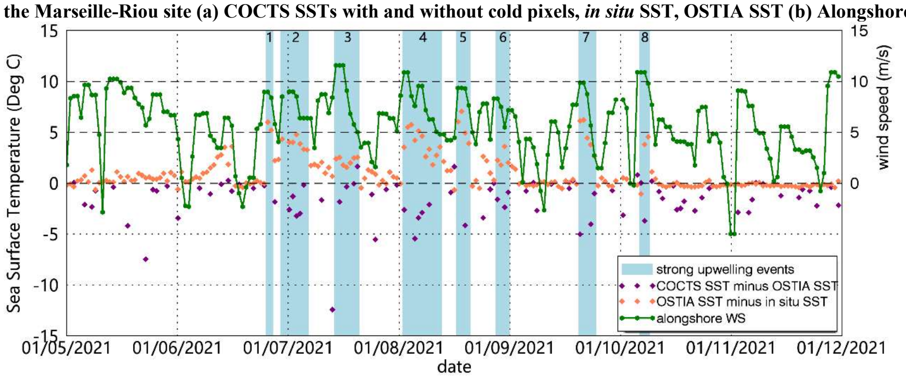

Figure 12: The time series of the COCTS SST minus OSTIA SST, OSTIA SST minus *in situ* SST, and alongshore wind speed at the Marseille-Riou site.

3.3.2 Relationship between COCTS-OSTIA SST difference and alongshore wind speed in upwelling areas

Because of the relationship between COCTS SST minus OSTIA SST and the alongshore wind speed, we consider setting a dynamic threshold according to this relationship. However, just the information from one point is not representative. To further analyze the relationship, we extend to the areas where upwelling may occur. OSTIA SST changes in the upwelling area, even if not as intense as the *in situ* SST, so the monthly variation of the OSTIA SST is used to determine the upwelling area. Because July and August have the most upwelling events, we just focus on the monthly variation of this two months. Fig. 13 shows the images and their corresponding histograms of the spatial distribution of the OSTIA monthly standard deviation in July and August. There are more pixels with relatively larger standard deviations in the near-land area, which corresponds to the upwelling area. The near-land areas (30 km from the land) with the OSTIA standard deviation greater than 1.5 °C in July and August are merged as the area influenced by upwelling.

https://doi.org/10.5194/egusphere-2026-5436
Preprint. Discussion started: 25 September 2026

The pixels within 1 km of the land in the probable upwelling areas in 16 strong upwelling days are chosen for analyzing the relationship between the OSTIA SST minus COCTS SST and the alongshore wind speed. The maximum alongshore wind speed of 6 to 54 hours (with a 6-hour interval applied) before the SST is used to analyze the correlation with the SST difference respectively. According to Odic et al. (2022), the conclusion that SST cooling lags strong wind by 6 to 54 hours is derived from observations at coastal sites. Therefore, it is better to apply the pixels near-land when we want to make the threshold by the relationship.

An alongshore wind speed of 5.84 m/s is the upwelling driving threshold (Odic et al., 2022). The pixels with the alongshore wind speed of less than 5.84 m/s are not considered as the wind driving upwelling pixels. The pixels with the values of the COCTS SST minus OSTIA SST less than -6 °C are not selected as the upwelling pixels for the relationship analysis because of the probable cloud cover.

OSTIA SST does not always have a large difference from the *in situ* SST (for instance in event 3) in strong upwelling events. Therefore, for most pixels, it is more reasonable to analyze the relationship of the largest difference between COCTS SST and OSTIA SST (at each small wind speed bin) with the alongshore wind speed and use the largest differences as the thresholds. The pixels smaller than the lower quartile of the differences in every alongshore wind speed bin of 0.5m/s are selected. The correlation coefficients are calculated by the lower quartile of the COCT SST minus OSTIA SST values and the alongshore wind speed.

Fig. 14 shows the correlation coefficients with different time lag of the SST relative to the alongshore wind speed. We can see the most relevant one is correlation coefficient when the time lag is 48, with a correlation coefficient of -0.507 ($p = 1.02 \times 10^{-5}$). Fig. 15 shows the relationship between the lower quartile of the COCT SST minus OSTIA SST values and the alongshore wind speed (the time lag is 48 hours). The blue line shows a linear regression to the wind speed data. The box is the area where the line minus 1°C or add 1°C covers. We apply this line minus 1°C as the dynamic threshold to cover more pixels with smaller values of COCTS SST minus OSTIA SST.

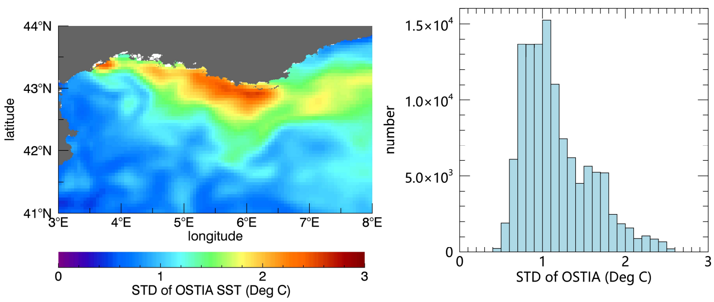

(a) (b)

https://doi.org/10.5194/egusphere-2026-5436
Preprint. Discussion started: 25 September 2026

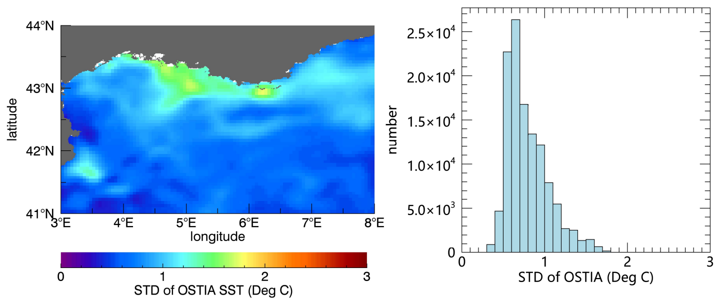

(c) (d)

Figure 13: Spatial distribution and corresponding histograms of monthly OSTIA SST standard deviation in July (a) (b) and August (c) (d)

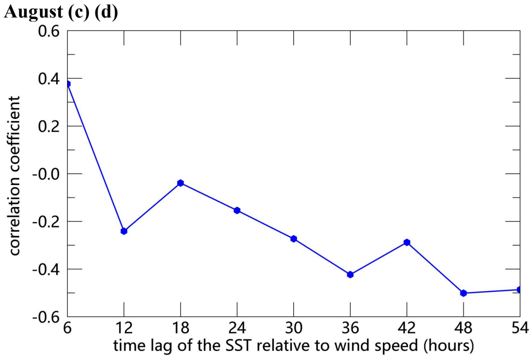

Figure 14: The correlation coefficients with different time lag of the SST relative to the alongshore wind speed.

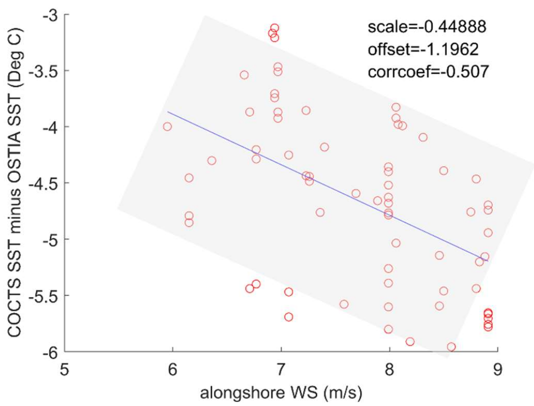

Figure 15: The relationship between the lower quartile of the COCT SST minus OSTIA SST values and the alongshore wind speed (The time lag is 48 hours).

https://doi.org/10.5194/egusphere-2026-5436
Preprint. Discussion started: 25 September 2026

3.3.3 The performance of reconstructed COCTS SST after improvement

We apply the threshold in probable upwelling areas from July to October, retaining more cold pixels. Fig. 16 shows the COCTS L3 SST before and after improvement on August 18 and October 8, respectively. More cold upwelling pixels misclassified as cloud are retained. The total availability is 40.10%, about 2% greater than the previous value (38%).

We input the improved COCTS L3 SST to the DINEOF for reconstruction. The COCTS L3 SST images with an availability of less than 5% (spatial dimension) and the pixels with an availability of less than 2% (time dimension) are removed. In spatial dimension the threshold is increased to 5%, which is to avoid spikes caused by the introduction of cold pixels. The number of optimal EOF modes for DINEOF reconstruction is 10. Fig. 17 shows the reconstructed COCTS L4 SST before and after improvement. Table 3 shows the difference between the COCTS SST and iQuam SST before and after improvement. For clear pixels before reconstruction, the standard deviation with improvement is 0.04℃ higher than the original. For the standard deviation of clear and cloud pixels after reconstruction, only 0.01 ℃ and 0.03 ℃ greater than the results before. Fig. 18 shows the spatial distribution of the difference between the COCTS and iQuam SSTs (with improvement). Fig. 19 shows the scatter plot of COCTS and iQuam SSTs (with improvement).

Fig. 20 shows the time series of the COCTS SSTs before and after reconstruction and the *in situ* SST (with improvement) at the three sites. We can see in upwelling events, reconstructed COCTS L4 SSTs are more consistent with the *in situ* SST than before, especially in events 4 ,5, 7 and 8. In event 4, the difference between the reconstructed COCTS L4 SST comes close to the *in situ* SST at the Marseille-Riou and CapVieux sites, and the difference from *in situ* SST at the Cassis site is reduced from more than 2 ℃ to around 1 ℃. In event 5, the differences are reduced from 4- 7 ℃ to 0.5-2 ℃ at the three sites, which is a significant improvement. In events 7 and 8, there are still differences of 1 to 4℃ at the three sites. However, compared to the results before improvement (the differences are even 6℃ at the CapVieux site), they still show a large improvement. The results show that the retained cold pixels contribute to the DINEOF process, not only to the days and positions that the pixels are located but also to the surrounding pixels and days.

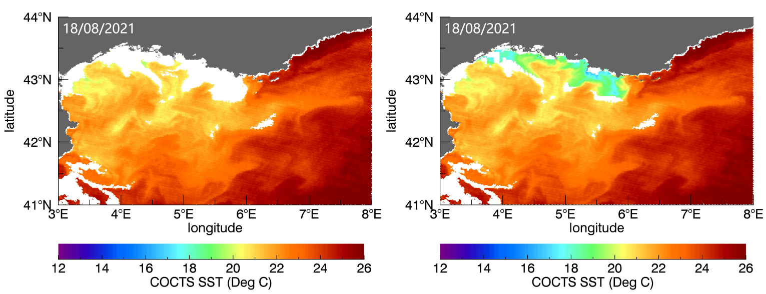

(a) **(b)**

https://doi.org/10.5194/egusphere-2026-5436
Preprint. Discussion started: 25 September 2026

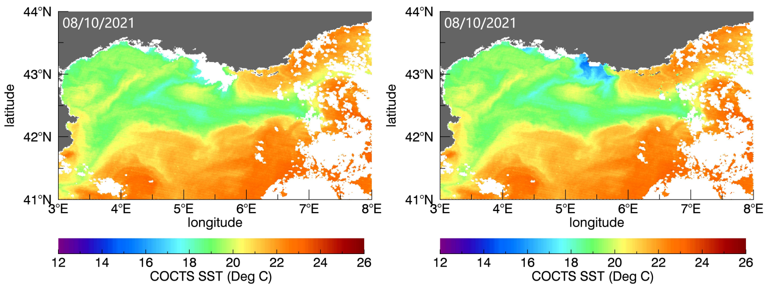

(c) (d)

Figure 16: The COCTS L3 SST before and after improvement (a) and (b) August 18 (c) and (d) October 8.

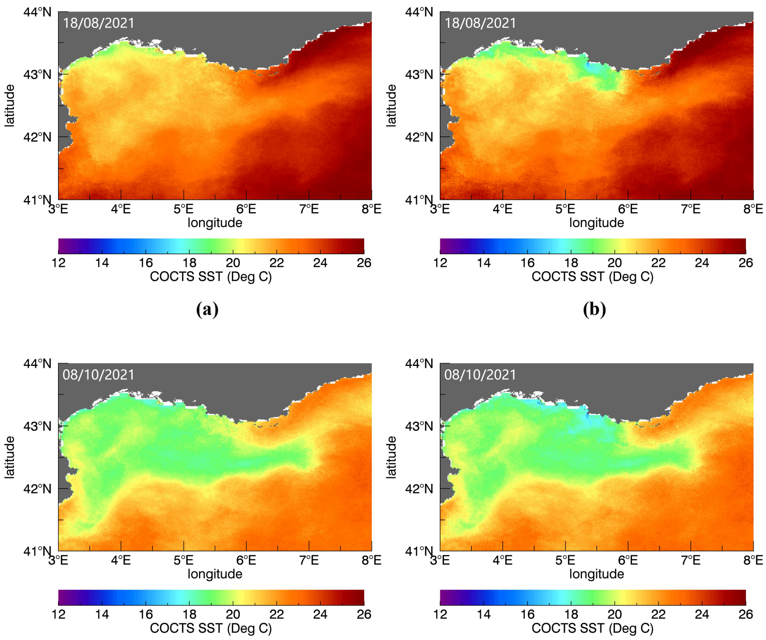

(c) (d)

Figure 17: The reconstructed COCTS L4 SST before and after improvement (a) and (b) August 18 (c) and (d) October 8.

https://doi.org/10.5194/egusphere-2026-5436
Preprint. Discussion started: 25 September 2026

Table 3: The difference between the COCTS SST and iQuam SST (before and after improvement).

		Bias (°C)	STD (°C)	Med. (°C)	RSD (°C)	No.
Before improvement	clear pixels before DINEOF	0.01	0.59	0.01	0.53	914
	clear pixels after DINEOF	0.03	0.58	0.04	0.54	914
	cloud pixels after DINEOF	-0.11	0.67	-0.10	0.67	1660
After improvement	clear pixels before DINEOF	-0.02	0.63	-0.01	0.54	947
	clear pixels after DINEOF	-0.01	0.59	0.01	0.54	947
	cloud pixels after DINEOF	-0.10	0.70	-0.09	0.69	1526

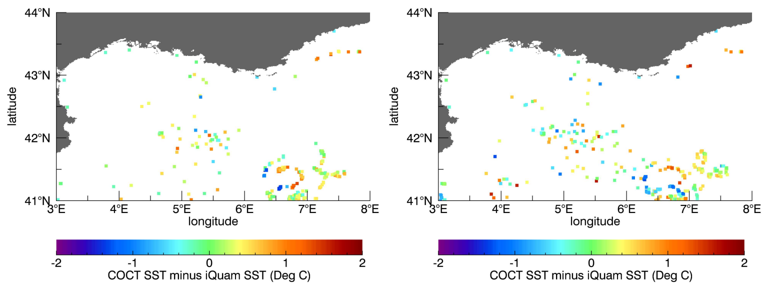

(a) **(b)**

Figure 18: The spatial distribution of the difference between the COCTS and iQuam SSTs (with improvement) (a) clear pixels (b) cloud pixels.

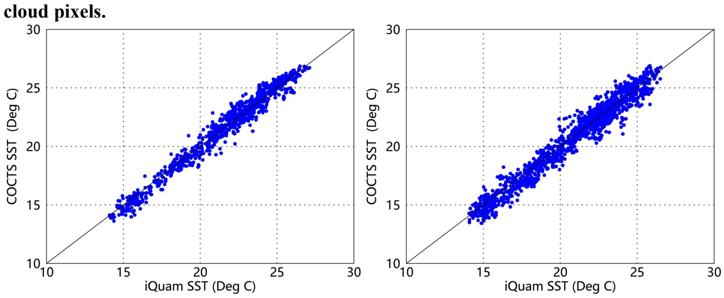

(a) **(b)**

Figure 19: The scatter plot of COCTS and independent iQuam SSTs (with improvement) (a) clear pixels (b) cloud pixels.

https://doi.org/10.5194/egusphere-2026-5436
Preprint. Discussion started: 25 September 2026

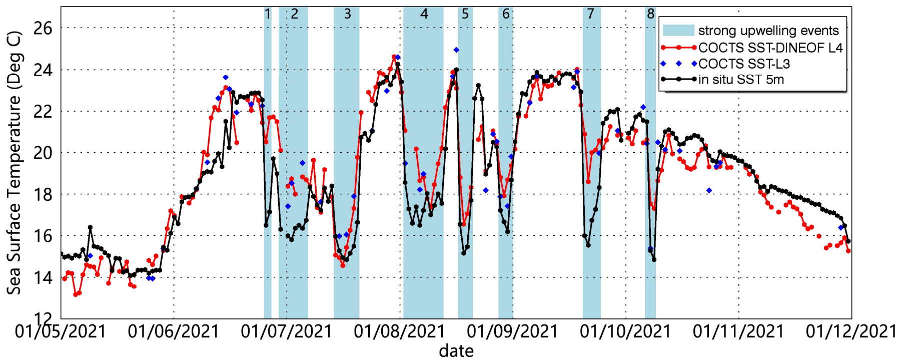

(a)

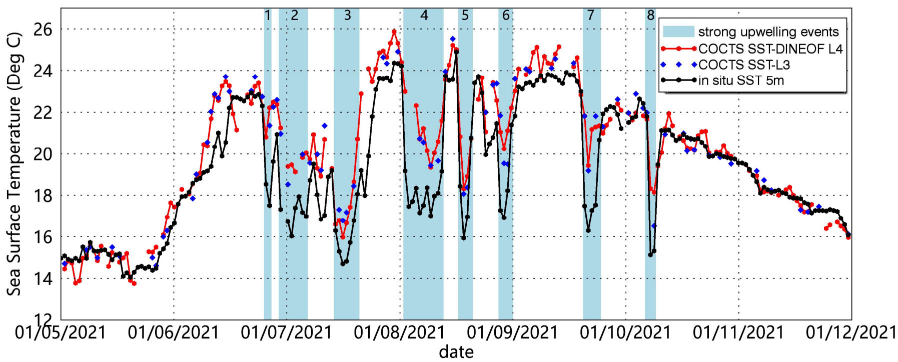

(b)

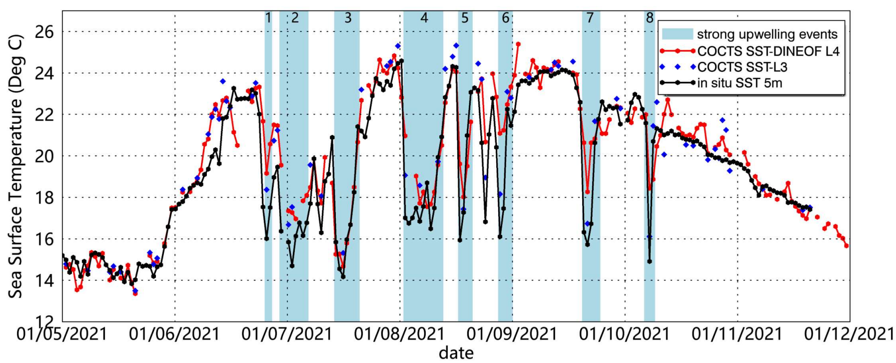

(c)

Figure 20: The time series of the COCTS SSTs before and after reconstruction and the *in situ* SST (With improvement) (a) Marseille-Riou (b) Cassis (c) CapVieux.

4 Conclusion

In this research, the COCTS SST is applied to analyze the SST cooling phenomenon in strong upwelling events in the Gulf of Lion.

Firstly, DINEOF is applied to reconstruct COCTS L3 SST. The validation results for reconstructed COCTS L4 SST show that the DINEOF performs well on COCTS L3 SST.

Secondly, the performance of the reconstructed COCTS L4 SST in upwelling events is analyzed. The results show that the reconstructed COCTS L4 SST characterizes most SST cooling events caused by upwelling, but not as intense as the *in situ* SST.

Thirdly, more cold COCTS L3 SST upwelling pixels misclassified as cloud are retained by applying a wind-informed dynamic threshold method based on the difference between COCT SST and OSTIA SST changing over the alongshore wind speed. After improvement, the availability of COCTS L3 SST increased from 38% to 40%. This 2% increase is not randomly distributed but represents the systematic recovery of cold upwelling pixels that were consistently flagged as bad data by the original quality control method. The standard deviation for clear pixels is 0.04 ℃ greater than the results before improvement, more valid cold COCTS SST pixels due to the strong upwelling are retained and the reconstructed COCTS L4 SST after improvement performs much better in the upwelling area.

DINEOF is applied to fill the gap caused by the cloud cover, which improves the ability of the analysis in long-time series. Although the COCTS L3 SST and reconstructed COCTS L4 SST have a relatively high accuracy even in the near-land area, there are some flagged cold pixels due to the upwelling events rather than the cloud cover, which is not conducive to the study of events such as upwelling. This misclassification issue widely exists in infrared satellite SST observations. For SST product producers, this kind of pixels could be retained with a relatively lower quality level, just for the users who want to research the upwelling events. In this study, we have made a preliminary attempt at it, and the results show that the improved COCTS L3 SST and reconstructed L4 SST have the potential to be applied to the analysis of the upwelling events. In the future, we will analyze the coastal strong upwelling events in other ocean areas to further validate the applicability of the method.

Code and data availability

The DINEOF code is available at https://github.com/aida-alvera/DINEOF. The *in situ* data is available at regional temperature observation network T-MEDNet(https://t-mednet.org/). The wind speed and OSTIA data are available at the Copernicus CMEMS(https://data.marine.copernicus.eu/products). The iQuam data is available at NOAA NESDIS STAR(https://www.star.nesdis.noaa.gov/socd/sst/iquam/data.html).

https://doi.org/10.5194/egusphere-2026-5436
Preprint. Discussion started: 25 September 2026

Author contributions

Z.L. Conceptualization, data curation, formal analysis, investigation, methodology, validation, visualization, writing (original draft and editing), writing (review and editing).

A.A-A. Conceptualization, methodology, resources, software, supervision, writing (review and editing).

A.B. Conceptualization, methodology, supervision, writing (review and editing).

N.B. Data curation, validation, writing (review and editing).

L.G. Funding acquisition, project administration, supervision, writing (review and editing).

N.X. Resources, writing (review and editing).

Competing interests

The authors declare that they have no conflict of interest.

Acknowledgements

The *in situ* data were provided by the regional temperature observation network T-MEDNet, https://t-mednet.org/. The wind speed and OSTIA data are from the Copernicus CMEMS, https://data.marine.copernicus.eu/products. The iQuam data is from NOAA NESDIS STAR, https://www.star.nesdis.noaa.gov/socd/sst/iquam/data.html.

Financial support

The work was supported by the Hainan Province Science and Technology Special Fund (ZDYF2024GXJS260), and also supported by the China Scholarship Council (202306330107).

References

Alvera-Azcárate, A., Barth, A., Rixen, M., and Beckers, J.-M.: Reconstruction of incomplete oceanographic data sets using empirical orthogonal functions: application to the Adriatic Sea surface temperature, Ocean Modelling, 9, 325–346, https://doi.org/10.1016/j.ocemod.2004.08.001, 2005.

Bakun, A.: Coastal upwelling indices, West Coast of North America, 1946-71, NOAA Technical Report NMFS SSRF-671, 103 pp., 1973.

Beckers, J.-M. and Rixen, M.: EOF calculations and data filling from incomplete oceanographic datasets, Journal of Atmospheric and Oceanic Technology, 20, 1839–1856, https://doi.org/10.1175/1520-0426(2003)020<1839:ECADFF>2.0.CO;2.

Bensoussan, N., Cebrian, E., Dominici, J.-M., Kersting, D. K., Kipson, S., Kizilkaya, Z., Ocaña, O., Peirache, M., Zuberer, F., Ledoux, J.-B., Linares, C., Zabala, M., Nardelli, B. B., Pisano, A., and Garrabou, J.: Using CMEMS and the Mediterranean Marine Protected Areas sentinel network to track ocean warming effects in coastal areas, J. Oper. Oceanogr., 12, S65–S73, 2019.

Ciappa, A. C.: The summer upwelling of the Eastern Aegean Sea detected from MODIS SST scenes from 2003 to 2015, International Journal of Remote Sensing, 40, 3105–3117, https://doi.org/10.1080/01431161.2018.1539272, 2019.

Csanady, G. T.: Intermittent 'full' upwelling in Lake Ontario, J. Geophys. Res., 82, 397–419, https://doi.org/10.1029/JC082i003p00397, 1977.

Emerson, S. R. and Hedges, J. I.: Chemical Oceanography and the Marine Carbon Cycle, Cambridge University Press, New York, United States of America, ISBN 978-0-521-83313-4, 2017.

Everson, R., Cornillon, P., Sirovich, L., and Webber, A.: An empirical eigenfunction analysis of sea surface temperatures in the western North Atlantic, Journal of Physical Oceanography, 27, 468–479, https://doi.org/10.1175/1520-0485(1997)027<0468:AEEAOS>2.0.CO;2, 1997.

Fragiacomo, C. and Parmiggiani, F.: An upwelling event in the central Mediterranean Sea detected by Quickscat and by AVHRR, International Journal of Remote Sensing, 23, 5151–5153, https://doi.org/10.1080/0143116021000016752, 2002.

García-Reyes, M., Largier, J. L., and Sydeman, W. J.: Under pressure: Climate change, upwelling, and eastern boundary upwelling ecosystems, Frontiers in Marine Science, 2, 109, https://doi.org/10.3389/fmars.2015.00109, 2015.

Garrabou, J., Gómez-Gras, D., Medrano, A., Cerrano, C., Ponti, M., Schlegel, R., Bensoussan, N., Turicchia, E., Marszalek, B., Puce, S., Raventos, N., Ribes, M., Hereu, B., Cerri, G., Cebrian, E., Zabala, M., and Kipson, S.: Monitoring climate-related responses in Mediterranean marine protected areas and beyond: Eleven standard protocols, 2022, https://doi.org/10.20350/digitalCSIC/14672.

Good, S., Fiedler, E., Mao, C., Martin, M. J., Maycock, A., Reid, R., Roberts-Jones, J., Searle, T., Waters, J., While, J., and Worsfold, M.: The Current Configuration of the OSTIA System for Operational Production of Foundation Sea Surface Temperature and Ice Concentration Analyses, Remote Sens., 12, 720, https://doi.org/10.3390/rs12040720, 2020.

He, R., Weisberg, R. H., Zhang, H., Muller-Karger, F. E., and Helber, R. W.: A cloud-free, satellite-derived, sea surface temperature analysis for the West Florida Shelf, Geophysical Research Letters, 30, 2003, https://doi.org/10.1029/2003GL017673.

Huang, Z. and Wang, X. H.: Mapping the spatial and temporal variability of the upwelling systems of the Australian south-eastern coast using 14-year of MODIS data, Remote Sensing of Environment, 227, 90–109, https://doi.org/10.1016/j.rse.2019.04.002, 2019.

Huang, Z., Hu, J., and Shi, W.: Mapping the coastal upwelling east of Taiwan using geostationary satellite data, Remote Sensing, 13, 170, https://doi.org/10.3390/rs13020170, 2021.

Høyer, J. L. and She, J.: Optimal interpolation of sea surface temperature for the North Sea and Baltic Sea, Journal of Marine Systems, 65, 176–189, 2007.

https://doi.org/10.5194/egusphere-2026-5436
Preprint. Discussion started: 25 September 2026

Kuo, N.-J., Zheng, Q., and Ho, C.-R.: Satellite observation of upwelling along the western coast of the South China Sea, Remote Sensing of Environment, 74, 463–470, https://doi.org/10.1016/S0034-4257(00)00138-3, 2000.

Kämpf, J. and Chapman, P.: Upwelling systems of the world: A scientific journey to the most productive marine ecosystems, Springer International Publishing, Switzerland, 443 pp., https://doi.org/10.1007/978-3-319-42524-5, 2016.

Lehmann, A. and Myrberg, K.: Upwelling in the Baltic Sea—A review, Journal of Marine Systems, 74, S3–S12, https://doi.org/10.1016/j.jmarsys.2008.02.010, 2008.

Li, J., Zhai, F., Liu, C., Gu, Y., Li, P., and Ye, G.: Wind-driven coastal upwelling causes synoptic-to-intraseasonal variations in tidal temperature variability near a strong shelf front in the northern South China Sea in summer, Frontiers in Marine Science, 12, 1553764, https://doi.org/10.3389/fmars.2025.1553764, 2025.

Li, Z., Guan, L., and Chen, R.: Sea surface skin temperature retrieval from HY-1D COCTS observations, Frontiers in Marine Science, 10, 1205776, https://doi.org/10.3389/fmars.2023.1205776, 2023.

Meneghesso, C., Seabra, R., Broitman, B. R., Wethey, D. S., Burrows, M. T., Chan, B. K. K., Guy-Haim, T., Ribeiro, P. A., Rilov, G., Santos, A. M., Sousa, L. L., and Lima, F. P.: Remotely-sensed L4 SST underestimates the thermal fingerprint of coastal upwelling, Remote Sensing of Environment, 237, 111588, https://doi.org/10.1016/j.rse.2019.111588, 2020.

Millot, C.: Wind induced upwellings in the Gulf of Lions, Oceanologica Acta, 2, 261–274, 1979.

Mourre, B., Reyes, E., Lorente, P., Santana, A., Hernández-Lasheras, J., Hernández-Carrasco, I., García-Jove, M., and Zarokanellos, N. D.: Intense wind-driven coastal upwelling in the Balearic Islands in response to Storm Blas (November 2021), State Planet, 1-osr7, 15, https://doi.org/10.5194/sp-1-osr7-15-2023, 2023.

Odic, R., Bensoussan, N., Pinazo, C., Taupier-Letage, I., and Rossi, V.: Sporadic wind-driven upwelling/downwelling and associated cooling/warming along Northwestern Mediterranean coastlines, Continental Shelf Research, 250, 104843, https://doi.org/10.1016/j.csr.2022.104843, 2022.

Pisoni, J. P., Rivas, A. L., and Piola, A. R.: Satellite remote sensing reveals coastal upwelling events in the San Matías Gulf—Northern Patagonia, Remote Sensing of Environment, 152, 270–278, 2014.

Rachman, H. A., Gaol, J. L., Syamsudin, F., and As-syakur, A.: Influence of coastal upwelling on sea surface temperature trends Banda Sea, IOP Conference Series: Earth and Environmental Science, 429, 012015, https://doi.org/10.1088/1755-1315/429/1/012015, 2020.

Rossi, V., Schaeffer, A., Wood, J., Galibert, G., Morris, B., Sudre, S., Roughan, M., and Waite, A. M.: Seasonality of sporadic physical processes driving temperature and nutrient high-frequency variability in the coastal ocean off southeast Australia, Journal of Geophysical Research: Oceans, 119, 445–460, https://doi.org/10.1002/2013JC009284, 2014.

Su, C., Chen, S., and Zhao, J.: Physically-aware deep learning for reconstructing gap-free sea surface temperature in the South China Sea, ISPRS Journal of Photogrammetry and Remote Sensing, 237, 253–270, https://doi.org/10.1016/j.isprsjprs.2026.04.016, 2026.

Thiébaut, M., Vonta, L., Benzo, C., and Guinot, F.: Characterization of the offshore wind dynamics for wind energy production in the Gulf of Lion, Western Mediterranean Sea, Wind Energy and Engineering Research, 1, 100002, https://doi.org/10.1016/j.weer.2024.100002, 2024.

Von Schuckmann, K., Le Traon, P.-Y., Smith, N., Pascual, A., Djavidnia, S., Gattuso, J.-P., Grégoire, M., Nolan, G., Aaboe, S., Fanjul, E. A., et al.: Copernicus marine service ocean state report, issue 3, Journal of Operational Oceanography, 12, S1–S123, https://doi.org/10.1080/1755876X.2019.1633075, 2019.

Wiafe, G. and Nyadjro, E. S.: Satellite observations of upwelling in the Gulf of Guinea, IEEE Geoscience and Remote Sensing Letters, 12, 1066–1070, https://doi.org/10.1109/LGRS.2014.2379474, 2015.

Xu, F. and Ignatov, A.: In situ SST quality monitor (iQuam), Journal of Atmospheric and Oceanic Technology, 31, 164–180, https://doi.org/10.1175/jtech-d-13-00121.1, 2014.